

Iterative Ultrasonic Signal and Image Deconvolution for Estimation of the Complex Medium Response

Zhiping Mu¹, Robert J. Plemmons², and Peter Santago II³

¹Section of Cardiovascular Medicine, Department of Internal Medicine, Yale University School of
Medicine, New Haven, CT06520, USA

²Departments of Mathematics and Computer Science, Wake Forest University, Winston-Salem,
NC27109, USA

³Department of Biomedical Engineering, Wake Forest University School of Medicine, Winston-Salem,
NC27157, USA

Abstract

The ill-conditioned inverse problem of estimating ultrasonic medium responses by deconvolution of RF signals is investigated. The primary difference between the proposed method and others is that the medium response function is assumed to be complex-valued rather than restricted to being real-valued. Derived from the complex medium model, complex Wiener filtering is presented, and a Hilbert transform related limitation to inverse filtering type methods is discussed. We introduce a non-parametric iterative algorithm, the least squares method with point count regularization (LSPC). The algorithm is successfully applied to simulated and experimental data and demonstrates the capability of recovering both the real and imaginary parts of the medium response. The simulation results indicate that the LSPC method can outperform Wiener filters and improve the resolution of the ultrasound system by factors as high as 3.7. Experimental results using a single element transducer and a conventional medical ultrasound system with a linear array transducer show that, despite the errors in pulse estimation and the noise in the RF signals, excellent results can be obtained, demonstrating the stability and robustness of the algorithm.

Keywords: ultrasound, deconvolution, complex medium response, Wiener filter, least squares method, point count regularization

I. INTRODUCTION

The primary purpose of medical ultrasonography is to retrieve information about the tissue on the path of the ultrasound pulses from the echoes. Theoretically, the exact echo waves are the solutions of the wave equation given the impedance map of the medium [Morse, 1986], [Insana, 1993], [Cho, 1993]. In practice it is well accepted that, one scan line of the received RF signal, $r(t)$ at time t , can be represented as [Cho, 1993], [Loupas, 1989], [Taxt, 2001]

$$r(t) = s(t) * p(t) + n(t), \quad (1)$$

where $s(t)$ is the medium response, $p(t)$ is the ultrasound pulse, $n(t)$ is the zero-mean Gaussian noise, and $*$ represents convolution. It is worthwhile noting that various naming conventions for $s(t)$ and $p(t)$ exist in the literature. $s(t)$ was referred to as the reflectivity function [Michailovich, 2002], [Adam, 2002], the tissue response [Abeyratne, 1995], and the spatial reflectance distribution [Carotenuto, 2002]. Aliases for $p(t)$ include the point spread function (PSF) [Michailovich, 2002], the impulse response [Jensen, 1993] and the ultrasound system response [Abeyratne, 1995].

In a B-mode ultrasound system, the demodulated signal or envelope is displayed in the image [Cho, 1993]. The resolution of such a system is usually defined as half of the $6dB$ pulse length (of its envelope) in the axial direction (considering round-trip travel), and the $6dB$ beam width in the lateral direction

[Loupas, 1989], [Shung, 1993]. Ultrasound pulses often span several cycles in time, thus increasing the center frequency of the transducer reduces pulse length and improves axial resolution. However, high frequency ultrasound systems suffer attenuation because the attenuation coefficient in soft tissue increases roughly linearly with the frequency [Cho, 1993]. Therefore, high frequency systems can not image structures deep inside the body.

The envelope displayed in a B-mode ultrasound image is a degraded representation of the $s(t)$ of the insonated tissues. Since the major degradation is due to the convolution with $p(t)$, it is believed that a better representation of $s(t)$ may be obtained by deconvolution. Beginning in the late 1970's and early 1980's, researchers have studied digital signal processing methods in order to improve the resolution of ultrasound B-scan images. Results of Gaussian-weighted inverse filtering [Hundt, 1980], Kalman filtering [Kuc, 1979], and Wiener filtering [Fatemi, 1980], [Robinson, 1984], [Vaknine, 1984], [Loupas, 1989], [Jensen, 1993], [Haider, 1998] were reported. Loupas and colleagues [Loupas, 1989] indicated possible artifacts introduced by deconvolution due to the use of envelope detected A-scan data and found that the results obtained with abdominal data were disappointing. Since demodulation is a nonlinear operation while deconvolution is linear, satisfactory results can only be obtained using RF signals [Loupas, 1989].

Several researchers have worked on a more ambitious approach, blind deconvolution, i.e., deconvolution without exact knowledge of the ultrasonic pulse [Abeyratne, 1995], [Taxt, 1999], [Taxt, 1997], [Taxt, 2001], [Michailovich, 2002], [Adam, 2002]. Their methods differ in the way to estimate the pulse. A higher order spectra based method [Abeyratne, 1995], cepstrum based methods [Taxt, 1997], a non-causal Markov chain based Bayesian phase unwrapping method [Taxt, 1999], [Taxt, 2001], a wavelet linear shrinkage [Adam, 2002], and a Laplacian distributed tissue reflectivity function (sparse structure of specular reflectors) assumption [Michailovich, 2002] have been used. While pulse estimation is an active research area and has attracted much attention, less effort was made to improve the deconvolution phase of the algorithms. In the approaches mentioned above, the Wiener filter was chosen to deconvolve the ultrasound signals.

Wiener filtering is a variation of the inverse filtering technique, a direct deconvolution method that minimizes mean square error (achievable only when good estimates of the power spectra of both the signal and noise are available). Iterative deconvolution methods [Banham, 1997], [Nagy, 1996] have attracted much attention during the past decade. Compared with inverse filtering, the primary advantages of iterative methods are the avoidance of explicit implementation of the inverse operator, the capability to monitor progress and to control noise effects with certain constraints, and the possible introduction of spatial adaptivity [Banham, 1997]. They usually generate better results at the expense of longer computing

times. Part of the reason that direct methods have been popular in the research of ultrasonic signal/image deconvolution is that researchers want real-time algorithms. However, a restored high resolution image offers additional information about fine details, which could be critical for some applications, even if not available in real time. Given the advances in computer technology, real-time implementation of iterative methods is likely close at hand.

In [Kaaresen, 1999], an iterative blind deconvolution algorithm, iterated window maximization (IWM), was reported in which the pulse and the reflectivity were estimated alternately. The pulse was estimated based on a prior assumption of autoregressive (AR) model and sparse reflector distribution. The reflectivity was represented as reflector locations and corresponding amplitudes. The amplitudes were estimated by linear least squares fitting given the locations. To estimate the locations, the data was partitioned into small windows. Within each window, all possible combinations of locations were tried according to predetermined transit sets, the optimal combination was selected, and the amplitude estimates were updated. The procedure continued until there was no change to either locations or amplitudes. Due to the nature of combinatorial search, the number of possible changes would increase nearly exponentially as the number of scatterers/reflectors increases. Therefore this algorithm would take a long time to converge if the scatterer/reflector configuration is complex. A more serious problem is that convergence to a global minimum is not guaranteed. That is, the predetermined local transit set may be in the neighborhood of a local minimum and the algorithm may converge to that local minimum.

The above work was based on the special assumption that the medium response is real valued, which may not be adequate to represent ultrasound signals. We propose an iterative deconvolution method based on a complex signal generation model [Mu, 2002] in which the RF echo signal is the real part of the convolution of the medium response, $\tilde{s}(t)$, and the pulse, $\tilde{p}(t)$, where $\tilde{s}(t)$ and $\tilde{p}(t)$ are complex. The observed RF pulse is actually the real part of $\tilde{p}(t)$, and the imaginary part can be obtained using the Hilbert transform. Letting subscripts r and i represent the real and imaginary parts, the RF signal is given by

$$\begin{aligned} r(t) &= \Re(\tilde{s}(t) * \tilde{p}(t)) + n(t) \\ &= s_r(t) * p_r(t) - s_i(t) * p_i(t) + n(t), \end{aligned} \quad (2)$$

where $j = \sqrt{-1}$ and \Re represents extraction of the real part of a complex number or function.

There are several reasons for adopting a complex medium response model. First, consider the reflection at the interface of two homogeneous media. In the convolution model, an interface is usually represented as a δ function [Kaaresen, 1999], [Demirli, 2001b]. Suppose an ultrasound wave is traveling through medium

1 toward medium 2. If the wave direction is perpendicular to the interface, the reflection coefficient is given by [Cho, 1993], [Shung, 1993], [Morse, 1986]

$$\frac{p_r}{p_i} = \frac{Z_2 - Z_1}{Z_2 + Z_1}, \quad (3)$$

where p_i and p_r are the incident and reflected acoustic pressure, respectively, and Z_1 and Z_2 are the characteristic acoustic impedances of the two media. In general, acoustic impedance is complex valued [Kinsler, 1982]. Hence the value of the δ function representing the interface is also complex.

The complex model also explains the phase shifting observed in experiments [Abeyratne, 1995], [Demirli, 2001a]. An ultrasound pulse is often represented as a high frequency cosine wave with a slowly varying envelope, where the pulse, $p(t)$, is the real part of a complex pulse $\tilde{p}(t)$,

$$\tilde{p}(t) = A(t)e^{j(\omega_0 t + \theta)}. \quad (4)$$

If the pulse is backscattered by a complex point scatterer represented as $\gamma e^{j\phi} \delta(t - \tau)$, the backscattered RF signal, $r(t)$, will be $\Re(\gamma A(t - \tau) e^{j(\omega_0(t - \tau) + \theta + \phi)})$. Therefore, in addition to the time delay determined by τ , which is actually determined by the location of the scatterer, there is a phase shift, ϕ , in the backscattered pulse. The effect of this phase shift is illustrated in Fig. 1.

The complex medium response assumption requires changes to the Wiener filters. When the medium response is assumed to be real valued, only the observed, real valued RF signals and pulses should be used. To estimate the complex medium response function, one has to use the complex RF signal and ultrasound pulse. In section II-A and [Mu, 2003], we show that the result of the conventional Wiener filter (using only the real valued RF signal and pulse) is the real part of the complex medium response estimated by the complex Wiener filter, and the imaginary part is the Hilbert transform of the real part. The Hilbert transform relationship between the real and imaginary parts of the medium response is unrealistic and superimposed by the band-pass property of the ultrasound pulse, a limitation of inverse filtering type of approaches.

The signal model represented by equation (2) is only for a single line of the RF signal, i.e., for 1-D signals. A similar model exists for 2-D signals, or images,

$$r(w, t) = \Re(\tilde{s}(w, t) * \tilde{p}(w, t)), \quad (5)$$

where the first index, w , represents the line number for linear array transducers and the angle number for angular array transducers (extension to model the novel higher-order arrays [Fernan, 2002] is also possible, adding another index to represent the elevation). Evidently, to deconvolve an ultrasonic RF image, a 2-D pulse pattern, $\tilde{p}(w, t)$, must be known. Rigorous studies show that for modern array transducers, the axial

pulse and the lateral beam pattern are not separable [Jensen, 1999]. The off-axis pulse is distorted due to the superimposition of emitted waves from multiple elements, even with apodization and dynamic aperture techniques, as shown later in section III.

Some primary publications on this topic based on complex medium response models include [Demirli, 2001a] and [Demirli, 2001b]. In these papers, a signal decomposition approach was taken that is similar to deconvolution. The echo signal was represented as superimposed Gaussian shape echoes, and the phase in the Gaussian echo model implied that the scatterer/reflector response is complex. The reflectivity was estimated using an expectation maximization (EM) based algorithm, and good results were obtained. However, this approach is strictly model based. Significant changes must be made if the pulse envelope is not Gaussian.

In ultrasound systems, the pulses are essentially band-pass filters. Some of the frequency components out of the pass band are virtually eliminated from the RF signals. Hence, small errors in the observed data, such as wide-band noise, might cause significant deviations in the deconvolution results. Thus, ultrasonic deconvolution is also ill-conditioned. Furthermore, the complex medium model introduces additional difficulty to the deconvolution, i.e., the deconvolution is mathematically underdetermined. As shown in equation (2), in addition to the observed pulse, $p_r(t)$, the imaginary part, $p_i(t)$, contributes to $r(t)$ too, a fundamental difference between the real and complex medium response models. If N samples of $r(t)$ are measured, there are N samples of s_r and N samples of s_i to determine, a system with N equations and $2N$ unknowns.

The imaginary part of a real valued band-pass signal can be obtained via the Hilbert transform of the signal based on the complex envelope and analytic signal theory [Goodman, 1985]. If the imaginary signal is used, the problem may appear to become well-determined, with $2N$ equations and $2N$ unknowns. However, the use of the imaginary signal does not improve the accuracy of the deconvolution, or make the deconvolution a determined problem. The reason is that the imaginary signal recovered in this way is entirely redundant. Since the Hilbert transform is a linear operation, and the imaginary part is computed from the real part by a linear operation, then the imaginary part of the signal is not an independent measurement and provides no more information than the real part alone. In other words, any solution to the real part will automatically solve the imaginary part. Hence, the complex deconvolution discussed in this paper still leads to an underdetermined inverse problem. Based on these considerations, only $r(t)$ is used in the algorithms.

We formulate the complex deconvolution of the RF signal as a problem of solving linear equations in section II-B. An iterative, least squares based method is introduced. The algorithm can be implemented

for both one-dimensional (1-D) and two-dimensional (2-D) problems. Simulated and experimental results are presented in section III.

II. THEORY

A. Modifications to Wiener filter due to the complex medium response assumption and associated Hilbert transform limitation

As indicated in the previous section, inverse filtering based methods, Wiener filters in particular, are the most commonly used approach for ultrasonic signal deconvolution. If the medium response is real valued, i.e., $\tilde{s}(t) = s_r(t)$, equation (2) becomes $r(t) = p_r(t) * s_r(t)$, and only the observed RF signals and pulses were used in inverse filtering. Letting $R_R(\omega)$ and $P_R(\omega)$ be the Fourier transform of $r(t)$ and $p_r(t)$, then the Fourier transform of the estimated real valued medium response, $\hat{S}(\omega)$, is given by

$$\hat{S}(\omega) = \frac{R_R(\omega)}{P_R(\omega)}, \quad (6)$$

assuming $P_R(\omega) \neq 0$ for all ω for simplicity. Please note that equation (6) yields the real valued medium response directly, without additionally taking the magnitude after Hilbert transform operation.

Equation (6) can only be applied to estimate real valued medium responses. Modifications to inverse filtering type of approaches (including Wiener filtering) are necessary when the medium response is complex valued. Let $\tilde{R}(\omega)$, $\tilde{P}(\omega)$, and $\tilde{S}(\omega)$ be the Fourier transforms of the complex RF signal, pulse, and medium response. Then, $\tilde{S}(\omega)$ estimated by inverse filtering should be given by

$$\tilde{S}(\omega) = \frac{\tilde{R}(\omega)}{\tilde{P}(\omega)}, \quad (7)$$

which is different from equation (6). In the appendix, we show that

$$\tilde{S}(\omega) = \begin{cases} \frac{1}{2}[\hat{S}(\omega) + j\mathcal{H}(\hat{S}(\omega))] & \text{if } \omega \neq 0, \\ \hat{S}(\omega) + j\mathcal{H}(\hat{S}(\omega)) & \text{if } \omega = 0, \end{cases} \quad (8)$$

where $\hat{S}(\omega)$ is computed from equation (6).

$R_R(\omega)$ and $P_R(\omega)$ are both Fourier transforms of real valued signals. Thus, $\hat{S}(\omega)$ is also the Fourier transform of a real valued signal, according to the conjugate symmetry property of the Fourier transform of real valued signals [Oppenheim, 1997]. The Hilbert transform of a real valued signal is still a real valued signal (this can be easily shown in either time domain or frequency domain). Hence, $\mathcal{H}(\hat{S}(\omega))$ is also the Fourier transform of a real valued signal. Therefore, equation (8) shows that $\tilde{S}(\omega)$ is the Fourier transform of a complex valued function, $\tilde{s}(t)$. Let

$$\tilde{s}(t) = \hat{s}_r(t) + j\hat{s}_i(t),$$

where $\hat{s}_r(t)$ and $\hat{s}_i(t)$ are the real and the imaginary parts of $\tilde{s}(t)$. Then $\hat{s}_r(t)$ has a Fourier transform of $\hat{S}(\omega)/2$, and $\hat{s}_i(t)$ has a Fourier transform of $\mathcal{H}(\hat{S}(\omega))/2$, and the imaginary part is the Hilbert transform of the real part of that function,

$$\hat{s}_i(t) = \mathcal{H}(\hat{s}_r(t)). \quad (9)$$

Equation (6) suggests that the real valued medium response can be computed by inverse filtering using only the real valued RF signal and pulse, without Hilbert transform. In practice, the so-called B-mode deconvolved image, which comprises the magnitudes of the complex envelope computed from the inverse filtering result by Hilbert transform, is displayed. This operation is actually evidence supporting the complex medium assumption, because it is not needed for real valued medium according to equation (6), and is exactly what the complex inverse filter, suggested by equations (8) and (9), does. Equation (6) yields an estimate of the real part of the complex medium response, \hat{s}_r , using the real part of the observed RF signal and the pulse. Then equation (9) suggests that the complex medium response can be obtained by taking the Hilbert transform of \hat{s}_r to compute \hat{s}_i . Obviously, the magnitude, $|\tilde{s}|$, is a better representation of the medium than the real part, \hat{s}_r alone. Because of the bandpass nature of the pulse and the presence of noise in the observed signal, replacing $1/P_R(\omega)$ in equation (6) by a Wiener Filter is widely applied to stabilize and optimize the performance of deconvolution. An example will be given later in Fig. 4 to show the effectiveness and superiority of this complex Wiener filter approach, modified for complex valued medium responses, over the conventional Wiener filters.

Earlier we indicated that medium responses are inherently complex. The Hilbert transform relationship between the real and imaginary parts does not apply to the medium response. Equation (9) is contradictory to that argument. However, \hat{s}_r and \hat{s}_i are estimated from the RF signal, and the Hilbert transform relationship holds for the RF signal. Hence, the loss of independence between the real and imaginary parts happens during signal generation. Equation (9) shows that inverse filtering based approaches are incapable of recovering the full information of a complex medium, a limitation to those methods.

B. An iterative deconvolution method — least squares with point count regularization (LSPC)

Written in discrete form, equation (2) becomes

$$\mathbf{r} = P_r \mathbf{s}_r - P_i \mathbf{s}_i + \mathbf{n}, \quad (10)$$

where \mathbf{r} and \mathbf{n} are $N \times 1$ vectors representing the N samples of the received RF signal and noise, \mathbf{s}_r and \mathbf{s}_i are both $N \times 1$ vectors representing the real and imaginary parts of the medium response function,

and P_r and P_i are $N \times N$ circulant matrices formed by the N samples of $p_r(t)$ and $p_i(t)$, respectively. Equation (10) can be rewritten as

$$\mathbf{r} = P\mathbf{s} + \mathbf{n} = \begin{pmatrix} P_r & -P_i \end{pmatrix} \begin{pmatrix} \mathbf{s}_r \\ \mathbf{s}_i \end{pmatrix} + \mathbf{n}, \quad (11)$$

where P is an $N \times 2N$ matrix, and \mathbf{s} is a $2N \times 1$ vector (in the case of images, \mathbf{r} , \mathbf{s}_r and \mathbf{s}_i are vectors formed by rows of the respective images, and P_r and P_i are block-circulant-and-circulant-block matrices [Gonzalez, 1992]).

Deconvolution is now formulated as a problem of solving a system of underdetermined linear equations. However, the direct solution by taking the inverse of P is not feasible because P is not a square matrix, and noise usually appears in \mathbf{r} . A least squares method is often applied under such circumstances. The idea is to find an \mathbf{s} that minimizes the least squares functional, J , which is given by

$$J = \frac{1}{2} \|\mathbf{r} - P\mathbf{s}\|^2. \quad (12)$$

For a ill-conditioned and underdetermined problem, regularization is usually employed to make it better-conditioned by modifying the functional J in equation (12) [Bertero, 1998]. For example, the functional with Tikhonov regularization may be written as [Bertero, 1998]

$$J = \frac{1}{2} \|\mathbf{r} - P\mathbf{s}\|^2 + \frac{\alpha}{2} \|\Lambda\mathbf{s}\|^2, \quad (13)$$

where α is a regularization parameter, and Λ is a linear smoothing operator [Bertero, 1998]. Unfortunately, our computations have shown that Tikhonov regularization is not effective. The minimization routines tend to use too many scatterers to approximate \mathbf{r} , and the resultant scatterers are widely spread in space. The reason is that the problem is extremely ill-conditioned. Mathematically, a large number of possible solutions exist. Thus, a stronger regularization approach is needed.

We propose a *Least Squares* method with *Point Count* regularization (LSPC), which uses the number of non-zero points in the solution as a constraint. This method seeks the least number of scatterers/reflectors to represent the actual scatterer/reflector distribution and reproduce the observed RF signal, minimizing the model complexity.

The general concept of point count constraints is not new, and similar ideas have been proposed within a variety of contexts. In image segmentation, the boundary length, which is equivalent to the number of edge points, has been used as a part of the energy functional in the well-known Mumford-Shah model [Morel, 1994]. Another example is the principle of *minimum description length* (MDL) [Duda, 2001], which finds application in various fields, such as pattern recognition, signal decomposition, and

machine learning, and has been used in [Demirli, 2001a] and [Demirli, 2001b]. The MDL principle states that the optimal description of the training data can be found by minimizing the sum of the model's algorithmic complexity and the description of the training data with respect to that model [Duda, 2001]. In deconvolution, the description complexity of the RF signal is proportional to the number of scatterers in the solution [Demirli, 2001a], which is the same concept as point count regularization. In [Demirli, 2001a] and [Demirli, 2001b], the algorithm starts with the assumption of one scatterer, and the number of scatterers is increased as the iterations proceed until the MDL starts to increase. It is a discrete implementation since the number of scatterers can only be integers. On the contrary, in the proposed LSPC method, the point count regularization is implemented as a continuous functional and therefore expected to be more flexible and robust.

In LSPC, the solution is found by minimizing the objective functional, J , defined as

$$J = J_{LS} + \alpha J_{PC}, \quad (14)$$

where J_{LS} is the least squares term as in equation (12), and J_{PC} is the point count term. The point count is carried out in two steps. The first is to determine how each sample point is counted, assigning a value between 0 and 1 to each. The second is to compute the sum of the values determined in the first step. J_{PC} is defined as $J_{PC} = \frac{1}{2} \mathbf{e}^T \mathbf{d}$, where \mathbf{e} is an $N \times 1$ summation vector whose elements are all 1s, and \mathbf{d} is the $N \times 1$ point determination vector. Each entry of \mathbf{d} corresponds to a sample point in space.

Before the computation of \mathbf{d} is introduced, we explain how the entry for each point is determined. The k th element of \mathbf{d} , is given by $d(k) = D(s_r(k) + js_i(k))$, where D is the point determination function. In principle, $D(u)$ (where u is a complex number) should be 0 if $|u|$ is 0, and 1 otherwise. However, such a point determination function is not continuous in the magnitude of u , hence not desirable for the minimization routine because the gradient of such a function is mostly zero and does not exist where $|u| = 0$. Instead, we use

$$D(u) = \frac{V^2(u)}{1 + V^2(u)} = 1 - \frac{1}{1 + V^2(u)}, \quad (15)$$

where $V(u) = |u|/\lambda$, and λ is a positive valued control parameter. This function is continuous and differentiable everywhere. $D(u)$ is 0 when $|u|$ is 0, 0.5 when $|u| = \lambda$, and approximately 1 when $|u| \gg \lambda$. Actually, the value of λ determines the inflection point of the function.

The equation to compute \mathbf{d} is a vector version of equation (15),

$$\mathbf{d} = \mathbf{v} ./ (1 + \mathbf{v}), \quad (16)$$

where $./$ represents element-wise division, and \mathbf{v} is an $N \times 1$ vector,

$$\mathbf{v} = \frac{[I, I]\mathbf{s} \cdot * \mathbf{s}}{\lambda^2} = \frac{\mathbf{s}_r \cdot * \mathbf{s}_r + \mathbf{s}_i \cdot * \mathbf{s}_i}{\lambda^2}, \quad (17)$$

$\cdot *$ is element-wise multiplication, and I is the $N \times N$ identity matrix.

The solution of the deconvolution problem often involves minimization methods such as a conjugate-gradient method or a quasi-Newton method, which requires the gradient of the objective functional. The gradient of J is given by

$$\begin{aligned} \nabla J &= \nabla J_{LS} + \alpha \nabla J_{PC} \\ &= P^T(P\mathbf{s} - \mathbf{r}) + \frac{\alpha}{\lambda^2} \mathbf{k} \cdot * \mathbf{k} \cdot * \mathbf{s}, \end{aligned} \quad (18)$$

where ∇ is the gradient operator, and \mathbf{k} is a column vector of the same size as \mathbf{s} such that

$$\mathbf{k} = \begin{pmatrix} 1./(1 + \mathbf{v}) \\ 1./(1 + \mathbf{v}) \end{pmatrix} = \begin{pmatrix} 1 - \mathbf{d} \\ 1 - \mathbf{d} \end{pmatrix}. \quad (19)$$

Parameter selection is usually critical to the success of iterative algorithms. Fortunately, the parameters involved in the LSPC algorithm can be chosen using simple heuristics. Usually the control parameter, λ , is given a very small value, much smaller than the expected scatterer strength (magnitude). The regularization parameter, α , governs the relative weight of the least squares and the point count regularization terms. Its value represents how much one expects the least squares to be reduced by adding an extra scatterer. The algorithm tends to overfit noise when α is too small and will ignore or miss some significant signals if α is too large. If the scatterers have comparable strengths, a single value can be used for the entire image. In this case, the value can be selected by trial and error. In general, α can be an image whose pixel values are computed according to the the observed B-mode image. In our experiments, we found the following empirical method usually yielded a good α . For an RF image, r , a B-mode image, b , can be obtained by demodulation. A local-maximum image, m , can be produced such that each pixel value in m is the maximum value in the neighborhood of the corresponding pixel in b . The size of the neighborhood is selected according to the size of the pulse, e.g., the 10dB footprint of the pulse. Then, for the n th pixel,

$$\alpha(n) = \frac{m^2(n)}{(KA)^2}, \quad (20)$$

where A is the maximum magnitude of the pulse, p , and K is a damping factor usually chosen between 10 and 20.

Although the introduction of point count regularization alleviates ill-conditioning and underdeterminedness, regularization alone does not guarantee efficient computation. To speed up the computation and to

improve accuracy, several methods can be employed; the implementation of these methods is problem dependent.

The starting point (initial solution guess) is an important aspect of iterative algorithms. The LSPC algorithm works well using solutions containing all zeros as the starting point, which is the case in the simulations and experiments unless indicated otherwise. While possessing certain limitations, the Wiener filter yields a good starting point for the LSPC algorithms. Normally a moderate or strong noise suppressing factor, γ , is used to give an *conservative* initial guess, avoiding severe noise amplification and ring artifacts that are difficult to recover.

Finite support (or region-of-support) has been shown to be a powerful constraint for inverse problems such as image restoration and reconstruction [Kundur, 1996]. The region of support can be from *a priori* knowledge or estimated from the measured data. Similarly, the envelopes of the signals may be used in a preprocessing step to provide a confidence map for the deconvolution algorithm. There are two ways to use the envelopes. One is to find the finite support by taking a threshold cut. The scatterer/reflector response is only allowed in the region where the envelope is greater than a threshold. Another is as a weighting factor for the point count function. There are many ways to apply the weighting factor, for example, the simplest is to use the reciprocal of the envelope, quantized into several levels, usually between 3 and 5.

The definition of the point determination function, $D(u)$, in equation (15) shows that in the region where $|u|$ is much greater than the relaxation parameter λ , the curve is flat. Therefore, if at one step the components of medium response $|\hat{s}(n)|$ are either 0 or much greater than λ , then $\|\nabla J_{PC}\|$, the norm of the gradient of J_{PC} , would be very small. As a result, the iteration might converge slowly. To speed up the computation, additional thresholding may be employed. After a few iterations, one may apply hard thresholding, i.e., the points where the magnitude of medium responses are lower than a threshold are set to 0, removing weak scatterers/reflectors. The threshold can be adaptively lowered while the computation proceeds. A more stable and less aggressive method is soft thresholding. Suppose the scatterer magnitude at the n th pixel is $|s(n)|$, and the threshold for that pixel is $\kappa(n)$, then the soft thresholded scatterer at the n th pixel always has an unchanged phase, and its magnitude is unchanged if $|s(n)| \geq \kappa(n)$, but is reduced to $|s(n)|^2/\kappa(n)$ otherwise. To establish the threshold image, κ , the deconvolved image magnitude, $|s|$, is first median filtered; then using the filtered image, a local maximum image is produced in a way similar to that of computing α ; finally, κ is computed by multiplying the local maximum image with a threshold factor that is usually between 0.05 and 0.3.

III. SIMULATION AND EXPERIMENTAL RESULTS

A. Simulations—1-D signals

Simulations were designed to illustrate the theories and to test the effectiveness of LSPC.

1) *Comparison with Tikhonov regularization:* Simulations were made using Matlab to compare LSPC to the least squares method with Tikhonov regularization (LSTik). In the simulations, the RF signals were generated by convolution of the known medium responses and pulses according to equation (1), and the deconvolution algorithms were invoked to find the medium responses. As shown in Fig. 2, Tikhonov regularization offered solutions containing widely distributed scatterers, while LSPC produced superior results. The original medium response contained two scatterers separated by four sample points (less than a half of a wavelength), no noise was added to the 128 point RF signal, and the sampling rate was 10 times the center frequency of the transducer. The linear operator, Λ , in LSTik was chosen as the identity matrix. (a) shows the original RF signal and the recovered RF signals, which are too similar to be discerned in the plot, implying that both results are mathematically the solution of equation (11). However, as shown in (b), LSPC found the correct solution while LSTik yielded a spatially widely-spread medium response (only the region of interest is plotted).

We indicated earlier in section I that for the results obtained with the complex Wiener filter, the imaginary part of the estimated medium response function is the Hilbert transform of the real part [Mu, 2003]. This unrealistic dependency is a limitation of inverse filtering based methods. Iterative methods usually generate better results because of the flexibility introduced by the choice of constraints. The result shown in Fig. 2 is a good example. LSPC recovered accurately the real and imaginary parts of the simulated scatterers, showing its superiority to Wiener filtering.

2) *Large noisy data segment:* LSPC generated excellent results even with noisy data, as shown in Fig. 3. The RF signal had 512 sample points, and the original medium response contained 20 randomly positioned point scatterers. The restored medium response comprised scatterer groups; each group consisted of 3-5 discrete scatterers. As shown in Fig. 3.b, the groups' positions were good indications of the original point scatterer locations. The magnitudes of the restored scatterers were smaller than that of the original ones because in the result the scattering sources were spread over the neighborhoods of the true scatterers.

B. Simulations—2-D images

Fig. 4 shows the result of a simulation designed (1) to verify the modifications to Wiener filters proposed in section II-A based on complex medium assumption; and (2) to test how well the LSPC

algorithm reduces speckle size. Some researchers have tested the effectiveness of their deconvolution algorithms by showing the reduced speckle size in the images, using the FWHM of the autocorrelation (or autocovariance) function of the image as a measurement of the speckle size [Abeyratne, 1995], [Jensen, 1993], [Taxt, 1995], [Taxt, 2001]. However, the reduced speckle size is not necessarily a direct proof of improved resolution. The major flaw of such a proof is the lack of strong indication that the image with reduced speckle size actually reflects the structure of the insonated medium. A way to avoid this is to generate images with known scatterer distributions so that it is easy to verify whether the resultant images faithfully represent the media.

The 1-D RF signals used in the previous simulations were the results of convolution of the known pulses and simulated medium response vectors, sometimes with additive noise. For image simulations, a more rigorous approach is taken. The RF signals (or images) were generated using the Field II simulator, a well accepted ultrasound simulator developed by Dr. Jørgen A. Jensen of the Technical University of Denmark using the concept of spatial impulse responses [Tupholme 1969], [Stepanishen, 1971]. Field II is capable of modeling a variety of modern array transducers. In this simulation, the simulated transducers were linear array transducers operated with dynamic focus, dynamic aperture, and apodization.

The original RF signals were generated by a simulated linear array transducer with a center frequency of $3MHz$ and sampled at $30MHz$ with a lateral line density of $0.2mm/line$, producing a 256×64 RF image. The software phantom was composed of an assembly of randomly positioned point scatterers, as shown in Fig. 4(b). The B-mode image acquired by the simulated transducer was logarithmically compressed and is shown in Fig. 4(a) (Although this is not a fully developed speckle image, the scatterer density is greater than one per resolution cell).

Shown in (c) and (d) are Wiener-filtered images. As indicated earlier, in most of the literature, Wiener filters were used for deconvolution, and the ultrasonic medium response functions were assumed to be real valued. Hence, the system responses (i.e., the pulse) and the RF signals used in those deconvolution methods were only their real parts. The Wiener filter is a variation of an inverse filter. Using our notation, the spectrum of the medium response estimated by conventional Wiener filtering, S_{CW} , is given by

$$S_{CW}(\omega) = \frac{P_R^*(\omega)R_R(\omega)}{|P_R(\omega)|^2 + \gamma}, \quad (21)$$

where the subscript CW stands for conventional Wiener, and γ is a noise suppressing parameter.

Estimating both the real and imaginary parts of the medium response, equations (6) and (8) depict an alternative to conventional Wiener filtering. In implementation, the inverse filter in equation (6), $1/P_R(\omega)$, can be replaced by the Wiener filter as well. In that case, $\hat{S} = S_{CW}$. Equation (8) suggests that, when the

medium response is complex valued, the imaginary part of medium response can be obtained by taking the Hilbert transform of the real part of medium response, which can be computed using equation (21). For convenience, this approach will be referred to as *complex Wiener filtering*. Clearly, the magnitude of the medium response represents the medium better than the real part alone.

The image in (c) (result of conventional Wiener filtering) has both positive and negative values, like an RF image. The image in (d) is the result of complex Wiener filtering, which is the magnitude of the analytic signal of (c). Just as B-mode ultrasound images are preferred to RF images in display, results of complex Wiener filtering (as in (d)) would be preferred to those of conventional Wiener filtering (as in (c)). Because the Field II simulator only accepts real values for the strength of the scatterers, intuitively the corresponding medium responses for those points might be considered as real values as well. However, even in this case, the complex Wiener filtering produced a better result, justifying the assumption of complex valued medium response functions and validating the modifications made to Wiener filtering in section II-A.

Evidently, the deconvolved image in Fig. 4(f) reflects very well the scatterer distribution shown in Fig. 4(b) and is much less blurred than the complex Wiener-filtered image in Fig. 4(d) (One may expect the Wiener-filtered image to be deblurred further by selecting a smaller noise suppressing factor γ in equation (21). However, Doing so will amplify the ring artifacts already evident in Fig. 4(d)).

The image autocovariances before and after deconvolution are plotted in Fig. 5, which shows that the LSPC deconvolved image has the smallest speckle size, and the LSPC algorithm improves the image resolution over the observed B-mode image and the image by factors of 3.3 and 1.3 laterally, 3.7 and 1.9 axially, respectively.

By minimizing the number of scatterers in the solution, the LSPC algorithm looks for a scatterer configuration from which the reflected waves build up constructively. In the case of speckles, the reflected waves build up mostly destructively. Therefore, the LSPC is not designed for speckle images. However, this should not be an obstacle of applying of the LSPC algorithm to ultrasonic imaging. The main purpose of image deconvolution is to improve resolution. The speckles represent a texture rather than a structure. In a speckle image, high intensity does not necessarily suggest presence of scatterer, and neither low intensity indicates lack of scatterer. In our point of view, the value of deconvolution is to unveil the fine details about previously blurred structures, such as closely located boundaries, not to generate finer speckles. And the LSPC algorithm is well suited for that cause, as illustrated by the simulation shown in Fig. 6. In this example, we imaged a software phantom composed of a segment of blood vessel and three weak lesions represented by point scatterers embedded in a speckle generating medium. The image

is corrupted by additive zero-mean Gaussian noise. The conventional B-mode image in (a) is very blurry. The two branches of the vessel appears as one thick structure, the lesion close to the vessel on the right is inseparable from the vessel, and the other two lesion near the bottom of the image merge as one large lesion. The Wiener-filtered image in (c) is moderately deblurred, and the ring artifact is already observable even with a conservative γ . However, the weak lesions remain indiscernible or barely discernible. The results of LSPC algorithm ((e) and (f)) display much increased contrast and improved resolution, and the weak lesions are well recognizable. When finite support and soft thresholding are turned off (in (e)), reduced ring artifacts and finer speckles exist in the background. In contrast, they are entirely removed when finite support and soft thresholding are employed (in (f)), yielding the best quality restoration. This example suggests that finite support and soft thresholding help to achieve higher contrast and better resolution. However, they result in an aggressive algorithm that removes low intensity background, hence should be used with caution if weak signals are also of interest.

We indicated in section I that the 2-D ultrasonic pulse is not separable and that the axial pulse is distorted off the center. The pulse shown in Fig. 6(b) is a good example. Visual observation finds that the middle white band (at $0.75mm$ axial and representing the positive peaks) appears straight, but the other two white bands curve away from the middle band, indicating lower frequency for off-center pulses and demonstrating the pulse distortion.

C. Experiments—1-D signals

Experimental RF signals were acquired to test the effectiveness of LSPC. A $20MHz$ transducer, Panametrics V373, with a $6dB$ passband of $17.9MHz$, was used and powered by a Panametric pulser/receiver 5900PR (Panametrics, Waltham, MA). The RF signal was sampled at $250MHz$ with a 9-bit depth by a CompuScope 8500 (Gage Applied Scientific, Montreal, Quebec) data acquisition card. The signals were then processed using Matlab.

In reality, the pulse, $\tilde{p}(t)$, is not completely known, but can be estimated by measuring the echo reflected from a surface. In the experiments, it was found that the Gaussian pulse model was too simple to represent the pulse. Instead, a non-symmetric Gaussian envelope, $A(t)$, was used:

$$A(t) = \begin{cases} e^{-\frac{(t-t_0)^2}{2\sigma_1^2}} & \text{if } t \geq t_0; \\ e^{-\frac{(t-t_0)^2}{2\sigma_2^2}} & \text{if } t < t_0. \end{cases} \quad (22)$$

An RF echo signal reflected from an aluminum plate placed at the focal plane was recorded, and a Matlab curve fitting routine, *lsqcurvefit*, was applied to estimate the envelope parameters, σ_1 and σ_2 , and the

center frequency, ω_0 . The result of pulse fitting is shown in Figure 7. Although pulse models were used in the experiments and simulations, they were not necessary, as the envelope could be numerical instead of parametric.

A difficulty with experimental data involves result verification, as the medium responses of the experimental materials are usually unknown. In our experiments, we used several plastic membranes of various thicknesses. For a plastic membrane, whose major echo generating structures are their two surfaces, the medium responses could be well represented by delta functions. However, because the sound speed is unknown, only the round trip time-of-flight (TOF) between the two surfaces could be measured and verified. To deal with this problem, we applied an indirect, frequency domain validation. If the medium responses of the materials can be modeled as two delta functions, then their power spectrums would contain a cosine function. If the total number of samples is N , and the round trip TOF between the two surfaces is d samples, then the period of the cosine function in the power spectrum, T , is given by

$$T = N/d. \quad (23)$$

The results of the experiments are shown in Figure 8. In the first row, the deconvolution algorithm gave two peaks separated by 7 to 8 points. In the estimated power spectrum, there appears to be two minima inside the pass band. However, the first minimum is very close to the edge and therefore is not reliable. The distance between the maximum and the second minimum, which is equal to $T/2$, is 8 points. According to equation (23), $d = N/T$. Since $N = 128$ in the data sets, the thickness is about 8 points based on the power spectrum estimation, which is in good agreement with the deconvolution result. In the second row, the two peaks in the deconvolution result are separated by 22 to 23 points. In the power spectrum, the average period of minima and maxima is 5.75 points, which gives an estimated thickness of 22.3 points. Once again, a good agreement is found between the deconvolution and power spectrum estimation.

D. Experiment—2-D image

Conventional medical ultrasound systems do not ordinarily provide access to the pre-demodulation signals, i.e., RF signals. Therefore, extensive study of the performance of the proposed LSPC algorithm on experimental images is difficult. Fortunately, with the help of Siemens Ultrasound Group (Issaquah, WA), we were able to acquire an RF image using a Siemens Antares ultrasound system and a Siemens VF7-3 linear array transducer operating at a center frequency of $3.3MHz$ and $40MHz$ sampling. LSPC was applied to that image, and the results are presented in Fig. 9.

Fig. 9(a) is the log-compressed B-mode image, which is an image of a group of resolution targets in the RMI-404GS phantom (Gammex Inc., Middleton, WI). This phantom incorporates tissue-mimicking gel to produce a speckle background, seen clearly in Fig. 9(a).

The targets in the phantom are made of 0.1mm diameter nylon lines, which are much smaller than the pulse length and width of the transducer. Therefore, the signals reflected from a target, if separable from those reflected from other targets, can be used as an approximation of the imaging ultrasound pulse. Considering the system variation and the presence of speckle background and noise, the pulse was estimated as an average of reflected RF signals from five of the targets on the right, marked by arrows in Fig. 9(a). The estimated pulse is shown in Fig. 10, which is not as smooth as the simulated pulse shown earlier and contains variations as a result of the speckle background in the acquired RF image.

The result of our LSPC deconvolution algorithm is shown in Fig. 9(d). Clearly the deconvolved image exhibits much higher resolution than the original B-mode image. Even the two targets with the smallest separation (top left), 0.25mm laterally, become barely discernible. Considering the poor estimate of ultrasound pulse, and the noisiness of the RF image, the quality of the result is very good and demonstrates of the robustness of the algorithm under fair experimental conditions.

IV. CONCLUSION AND DISCUSSION

We have presented a new method, LSPC, to process ultrasound echo signals in order to obtain a better estimation of the medium response and thus to retrieve more detailed information about the underlying structure of the material. LSPC is an iterative method that requires no parametric representation of the ultrasound pulse and is suitable for a variety of ultrasound systems. It is also flexible, with a few parameters to be chosen depending on the particular data set. The continuous-function implementation of the point count constraint further improves the stability of this algorithm. The algorithm was successfully applied to simulated and to experimental data, demonstrating the robustness of the algorithm and its capability to improve the ultrasound system resolution by factors up to 3.7.

As shown in section III, LSPC efficiently and accurately solves the complex deconvolution problems presented. However, the algorithm is not yet optimized, and there are a few parameters to be selected. From equation (14), one can see that the regularization parameter, α , defines the relative importance of the least squares errors and the number of scatterer sites, and should be selected according to the noise level and the echo signal power. While the empirical method to determine α , given by equation (20), performed well in simulations and experiments, further improvement may be achieved by engaging dynamic rather than static α s. For example, a large damping factor, K , may be used in the beginning

and decreased gradually throughout the iterations, or even different K values for different regions of the image can be used. Currently, λ is selected to be very small in order to make point determination function $D(u)$ close to the point count. Because the gradient of $D(u)$ is approximately 0 except in the region near λ (see equation (15)), a dynamic λ may be used in order to offer stronger “driving force” to the minimization routine. Still, there are many areas open for further research in the implementation. A thorough discussion of these issues will require further study of the algorithm.

A fundamental difference between ultrasound imaging and other modalities that justifies the use of point count regularization is that ultrasound imaging is a *differential* imaging technique. While the image pixel intensities represent local properties in other modalities, e.g., X-ray attenuation coefficients in CT [Cho, 1993], [Seeram, 2001], they represent the changes of acoustic impedance in ultrasound images. Echoes are generated when the pulse propagates through areas of inhomogeneity. In other words, ultrasound imaging is sensitive to the change, or gradient, of the tissue’s acoustic impedance. While local properties such as tissue attenuation coefficients exist everywhere inside the tissue, significant changes of tissue’s acoustic impedance, modeled as scatterers, are distributed much more sparsely in space.

As discussed before, LSPC may not be suitable for well developed speckle images (or signals) that are generated by a large number of non-resolvable scatterers, because in these images the backscattered signals from the individual scatterers build up destructively, and the true scatterer distributions may not be the most efficient solutions (with least number of scatterers). However, structures generating well developed speckles contain high spatial frequency information far beyond the recognition of the system. Deconvolution of the speckles may yield finer speckle patterns, which is only of cosmetic value because such speckles do not resemble the underlying echoic structures. Hence, improved resolution does not help much with speckle but reveals finer details about structures such as thin blood vessels or closely located lesions. The LSPC algorithm works very well in that regard, as demonstrated by the simulations and experiments. On the other hand, even though LSPC may sometimes not find the correct solutions, it may be possible to extract useful information from the solutions. For example, the solutions might have different features for images generated by different scatterer number densities. Further study is needed to extract features representing the scatterer distribution from the solutions.

In addition to medical ultrasound imaging, LSPC can be applied to ultrasound nondestructive testing (evaluation) and seismic processing, where reflectors can be modeled as isolated points, lines or surfaces. It is also suitable for astronomical imaging where the stars can be very well modeled as isolated points.

APPENDIX

Proof of Equation (8) Let $R_I(\omega)$ and $P_I(\omega)$ be the FTs of the imaginary RF signal and pulse. Then

$$\tilde{R}(\omega) = R_R(\omega) + jR_I(\omega), \quad (24)$$

$$\tilde{P}(\omega) = P_R(\omega) + jP_I(\omega). \quad (25)$$

In practice, $R_I(\omega)$ and $P_I(\omega)$ are computed from $R_R(\omega)$ and $P_R(\omega)$ by the Hilbert transform. Substituting equation (24) and (25) into equation (7), and using the fact that the Hilbert transform can be represented as a filter with a transfer function of $-j\text{sgn}(\omega)$ [Goodman, 1985] where sgn is the sign function, for $\omega \neq 0$,

$$\begin{aligned} \tilde{S}(\omega) &= \frac{R_R(\omega) + jR_I(\omega)}{P_R(\omega) + jP_I(\omega)} \\ &= \frac{R_R(\omega) + \text{sgn}(\omega)R_R(\omega)}{P_R(\omega) + \text{sgn}(\omega)P_R(\omega)} \\ &= \frac{2\mathcal{P}(R_R(\omega))}{2\mathcal{P}(P_R(\omega))} \\ &= \mathcal{P}\left(\frac{R_R(\omega)}{P_R(\omega)}\right), \end{aligned} \quad (26)$$

where \mathcal{P} represents the operation of preserving the positive part of the spectrum,

$$\mathcal{P}(X(\omega)) = \begin{cases} X(\omega) & \text{if } \omega > 0; \\ 0 & \text{otherwise.} \end{cases} \quad (27)$$

We now consider the right side of equation (8). Using equation (6), for $\omega \neq 0$,

$$\begin{aligned} \frac{1}{2}[\hat{S}(\omega) + j\mathcal{H}(\hat{S}(\omega))] &= \frac{1}{2}[\hat{S}(\omega) + \text{sgn}(\omega)\hat{S}(\omega)] \\ &= \mathcal{P}(\hat{S}(\omega)) \\ &= \mathcal{P}\left(\frac{R_R(\omega)}{P_R(\omega)}\right). \end{aligned} \quad (28)$$

Comparing equation (28) and (26), one can conclude that equation (8) holds for $\omega \neq 0$. When $\omega = 0$, both $R_I(\omega)$ and $P_I(\omega)$ are equal to zero, and $\mathcal{H}(\hat{S}(\omega)) = 0$. Hence, it is trivial to show that equation (8) holds for $\omega = 0$ as well.

ACKNOWLEDGMENT

The authors would like to thank Dr. Liexiang Fan of Siemens Ultrasound group for his help on RF data acquisition and Debra Stutz of Duke University for assistance on converting the data format. Special thanks goes to Dr. Jørgen A. Jensen of the Technical University of Denmark for developing and making available the Filed II simulator. The insightful and inspiring discussions with Dr. Gregg Trahey of Duke University are also highly appreciated.

Support for this study was provided in part by the Wake Forest Claude D. Pepper Older Americans Independence Center through NIA grant 3 P30 AG21332-01S1 from the National Institutes of Health, by the Air Force Office of Scientific Research under grant F49620-02-1-0107, and by the Army Research Office under grant DAAD19-00-1-0540.

REFERENCES

- [Abeyratne, 1995] U.R. Abeyratne, A.P. Petropulu, and J.M. Reid. Higher order spectra based deconvolution of ultrasound images. *IEEE Trans. Ultrason., Ferroelect., Freq. Contr.*, 42(6):1064–1075, 1995.
- [Adam, 2002] D. Adam and O. Michailovich. Blind deconvolution of ultrasound sequences using nonparametric local polynomial estimates of the pulse. *IEEE Trans. Biomed. Eng.*, 49(2):118–131, 2002.
- [Banham, 1997] M.R. Banham and A.K. Katsaggelos. Digital image restoration. *IEEE Signal Processing Mag.*, 14(2):24–41, 1997.
- [Bertero, 1998] M. Bertero and P. Boccacci. *Introduction to Inverse Problems in Imaging*. Institute of Physics Publishing Ltd., London, 1998.
- [Carotenuto, 2002] R. Carotenuto, G. Sabbi, and M. Pappalardo. Spatial resolution enhancement of ultrasound images using neural networks. *IEEE Trans. Ultrason., Ferroelect., Freq. Contr.*, 49(8):1039–1049, 2002.
- [Cho, 1993] Z. Cho, J.P. Jones, and M. Singh. *Foundations of Medical Imaging*. John Wiley & Sons, USA, 1993.
- [Demirli, 2001a] R. Demirli and J. Saniie. Model-based estimation of ultrasonic echoes, Part one: analysis and algorithms. *IEEE Trans. Ultrason., Ferroelect., Freq. Contr.*, 48(3):787–802, 2001.
- [Demirli, 2001b] R. Demirli and J. Saniie. Model-based estimation of ultrasonic echoes, Part two: nondestructive evaluation. *IEEE Trans. Ultrason., Ferroelect., Freq. Contr.*, 48(3):803–811, 2001.
- [Duda, 2001] R.O. Duda, P.E. Hart, and D.G. Stork. *Pattern Classification*. John Wiley and Sons, 2001.
- [Fatemi, 1980] M. Fatemi and A.C. Kak. Ultrasonic B-scan imaging: Theory of image formation and a technique for restoration. *Ultrason. Imag.*, 2:1–47, 1980.
- [Fernan, 2002] A.T. Fernandez, J.J. Dahl, K. Gammelmark, D.M. Dumont, and G.E. Trahey. High resolution ultrasound beamforming using synthetic and adaptive imaging techniques. *Proc. 2002 IEEE Int’l Sympo. Biomed. Imaging*, pages 433–436, 2002.
- [Gonzalez, 1992] R.C. Gonzalez and R.E. Woods. *Digital Image Processing*. Addison-Wesley, 2nd edition, 1992.
- [Goodman, 1985] J. W. Goodman. *Statistical Optics*. John Wiley & Sons, USA, 1985.
- [Haider, 1998] B. Haider, P.A. Lewin, and K.E. Thomenius. Pulse elongation and deconvolution filtering for medical ultrasonic imaging. *IEEE Trans. Ultrason., Ferroelect., Freq. Contr.*, 45(1):98–113, 1998.
- [Hundt, 1980] E.E. Hundt and E.A. Trautenberg. Digital processing of ultrasonic data by deconvolution. *IEEE Trans. Sonics and Ultrason.*, SU-27(5):249–252, 1980.
- [Insana, 1993] M.F. Insana and D.G. Brown. Acoustic scattering theory applied to soft biological tissues. In K.K. Shung and G.A. Thieme, editors, *Ultrasonic Scattering in Biological Tissues*. CRC Press, USA, 1993.
- [Jensen, 1999] J.A. Jensen. *Linear description of ultrasound imaging systems—Notes for summer school on advanced ultrasound imaging*. 1999.
- [Jensen, 1993] J.J. Jensen, J. Mathorne, T. Gravesen, and B. Stage. Deconvolution of in-vivo ultrasound B-mode images. *Ultrason. Imag.*, 15:122–133, 1993.
- [Kaaresen, 1999] K.F. Kaaresen and E. Bølviken. Blind deconvolution of ultrasonic traces accounting for pulse variance. *IEEE Trans. Ultrason., Ferroelect., Freq. Contr.*, 46(3):564–573, 1999.
- [Kinsler, 1982] L.E. Kinsler, A.R. Frey, A.B. Coppens, and J.V. Sanders. *Fundamentals of Acoustics*. John, Wiley & Sons, USA, 1982.
- [Kuc, 1979] R.B. Kuc. Application of Kalman filtering technique to diagnostic ultrasound. *Ultrason. Imag.*, 1:105–120, 1979.

- [Kundur, 1996] D. Kundur and D. Hatzinakos. Blind image deconvolution. *IEEE Signal Processing Magazine*, 13(3):43–64, 1996.
- [Loupas, 1989] T. Loupas, S.D. Pye, and W.N. McDicken. Deconvolution in medical ultrasonics: practical considerations. *Phys. Med. Biol.*, 34(11):1691–1700, 1989.
- [Michailovich, 2002] O. Michailovich and D. Adam. Blind deconvolution of ultrasound images using partial spectral information and sparsity constraints. In *IEEE International Symposium on Biomedical Imaging*, pages 1055–1058, 2002.
- [Morel, 1994] J. Morel and S. Solimini. *Variational methods in image segmentation*. Birkhäuser, 1994.
- [Morse, 1986] P.M. Morse and K.U. Ingard. *Theoretical Acoustics*. Princeton University Press, USA, 1986.
- [Mu, 2003] Z. Mu. *Ultrasonic signal processing and Tissue Characterization*. PhD thesis, Wake Forest University School of Medicine, 2003.
- [Mu, 2002] Z. Mu, R.J. Plemmons, D.M. Herrington, and P. Santago. Estimation of complex medium responses by deconvolution. *Proc. 2002 IEEE Int'l Symp. Biomed. Imag.*, pages 1047–1150, 2002.
- [Nagy, 1996] J.G. Nagy, R.J. Plemmons, and T.C. Torgersen. Iterative image restoration using approximate inverse preconditioning. *IEEE Trans. Image Processing*, 5(7):1151–1162, 1996.
- [Oppenheim, 1997] A.V. Oppenheim and A.S. Willsky. *Signals & Systems*. Prentice Hall, USA, 2nd edition, 1997.
- [Robinson, 1984] D.E. Robinson and W. Wing. Lateral deconvolution of ultrasonic beams. *Ultrason. Imag.*, 6:1–12, 1984.
- [Seeram, 2001] E. Seeram. *Computed Tomography—Physical Principles, Clinical Applications and Quality Control*. W.B. Saunders Company, 2nd edition, 2001.
- [Shung, 1993] K.K. Shung and G.A. Thieme. *Ultrasonic Scattering in Biological Tissues*. CRC Press, USA, 1993.
- [Stepanishen, 1971] P.R. Stepanishen. Transient radiation from pistons in an infinite planar baffle. *J. Acoust. Soc. Am.*, 49:1629–1638, 1971.
- [Taxt, 1995] T. Taxt. Restoration of medical ultrasound images using two-dimensional homomorphic deconvolution. *IEEE Trans. Ultrason., Ferroelect., Freq. Contr.*, 42(4):543–554, 1995.
- [Taxt, 1997] T. Taxt. Comparison of cepstrum-based methods for radial blind deconvolution of ultrasound images. *IEEE Trans. Ultrason., Ferroelect., Freq. Contr.*, 44(3):666–674, 1997.
- [Taxt, 1999] T. Taxt and G.V. Frolva. Noise robust one-dimensional blind deconvolution of medical ultrasound images. *IEEE Trans. Ultrason., Ferroelect., Freq. Contr.*, 46(2):291–299, 1999.
- [Taxt, 2001] T. Taxt and J. Strand. Two-dimensional noise-robust blind deconvolution of ultrasound images. *IEEE Trans. Ultrason., Ferroelect., Freq. Contr.*, 48(4):861–866, 2001.
- [Tupholme 1969] G.E. Tupholme. Generation of acoustic pulses by baffled plane pistons. *Mathematika*, 16:209–224, 1969.
- [Vaknine, 1984] R. Vaknine and W.J. Lorenz. Lateral filtering of medical ultrasonic B-scans before image generation. *Ultrason. Imag.*, 6:152–158, 1984.

LIST OF FIGURE CAPTIONS

Fig. 1 Effect of phase shift. Solid line and dash line are two pulses with the same envelope but different phases. The dash-dot line is the envelope.

Fig. 2 Results of LSPC and LSTik methods. (a) RF signals and envelope. (b) Magnitude of medium responses. The true medium response is shown as circles. The LSPC and the LSTik results are shown with '+'s and solid line, respectively. Although only the magnitudes of the results are shown here, the LSPC method indeed accurately recovered both the real and imaginary parts of the solution.

Fig. 3 Results of LSPC method with noisy data. (a) RF signals. The solid line is the observed signal and the dashed line is the recovered signal. (b) Magnitude of medium responses. The original medium response is shown as crosses and the solid line is the result of LSPC.

Fig. 4 The result of LSPC deconvolution of an image of randomly positioned scatterers. (a) Simulated B-mode image. (b) Original scatterer distribution. The intensity of the image represents the strength of scatterers. (c) Results of conventional Wiener filtering using only the real parts of the RF signal and pulse. (d) The magnitude of estimated medium response function using complex Wiener filtering given by equation (8). (e) The regularization parameter image, α , given by equation (20). (f) LSPC restored image after deconvolution with 40 iterations followed by median filtering. Finite support and soft thresholding are applied. The damping factor, K in equation (20), is 15, and the thresholding factor is chosen as 0.25.

Fig. 5 Normalized image autocovariance functions before and after deconvolution. (a) Autocovariance functions with axial shift. (b) Autocovariance functions with lateral shift. The dashed line represents the function of the B-mode image (Fig. 4(a)), the dash-dot line is for the image after Wiener filtering (Fig. 4(d)), the solid line is for the image after LSPC deconvolution (Fig. 4(f)), and the dotted line marks the half maximum of the functions. The FWHM of the three autocovariance functions are $4.6mm$, $1.8mm$, and $1.4mm$ laterally, and $0.85mm$, $0.44mm$ and $0.23mm$ axially. These numbers show that the LSPC algorithm improves the image resolution over the observed B-mode image and the Wiener filtered image by factors of 3.3 and 1.3 laterally, and 3.7 and 1.9 axially.

Fig. 6 The result of LSPC deconvolution of an noisy image of a blood vessel software phantom with speckle background. (a) Simulated B-mode image of a segment of blood vessel, a scatterer beneath the vessel on the right, and two scatterers near the bottom. The image is log-compressed to a 40dB

dynamic range. The maximum intensity of the image is about 15, and the standard deviation of the additive Gaussian noise is 0.15. (b) The incident ultrasonic pulse. (c) The magnitude of estimated medium response function using complex Wiener filtering given by equation (8) that serves as the initial guess in the LSPC algorithm. (d) The regularization parameter image, α , given by equation (20). (e) and (f) are results of two implementations of the LSPC algorithm. Both use the Wiener filtered image as the initial guess and apply median filtering after iterations. (e) is obtained after 30 iterations without the use of finite support or soft thresholding. (f) is the result of 20 iterations with finite support and soft thresholding. The damping factor is 15, and the thresholding factor is chosen as 0.25.

Fig. 7 The pulse of the V373 transducer and its spectrum. (a) The result of pulse fitting. The solid line is the measured echo signal and the dashed line is the curve-fitted pulse. (b) The magnitude of the FFT of the pulse.

Fig. 8 Experimental results using plastic membranes with different thicknesses. Each row is a set of experimental data. The left column contains the RF echo signals. The results of deconvolution using LSPC method are shown in the middle column and the estimated power spectra (the low frequency half) of the medium responses in the right column.

Fig. 9 Experimental result of LSPC algorithm. (a) Log-compressed B-mode phantom image acquired by a Siemens Antares medical ultrasound system. The phantom used is the RMI-404GS phantom. (b) The diagram of the targets in the imaged phantom. (c) The regularization parameter image, α , given by equation (20). (d) Deconvolved image after 40 LSPC iterations followed by median filtering. Neither finite support nor the soft thresholding technique was used in this experiment.

Fig. 10 Ultrasound pulse estimated from Fig. 9(a).

FIGURES

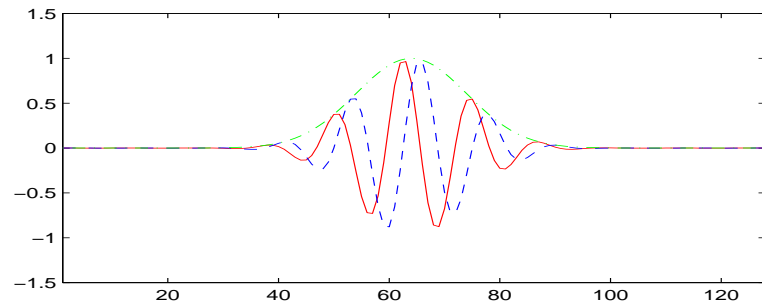


Fig. 1. Effect of phase shift. Solid line and dash line are two pulses with the same envelope but different phases. The dash-dot line is the envelope.

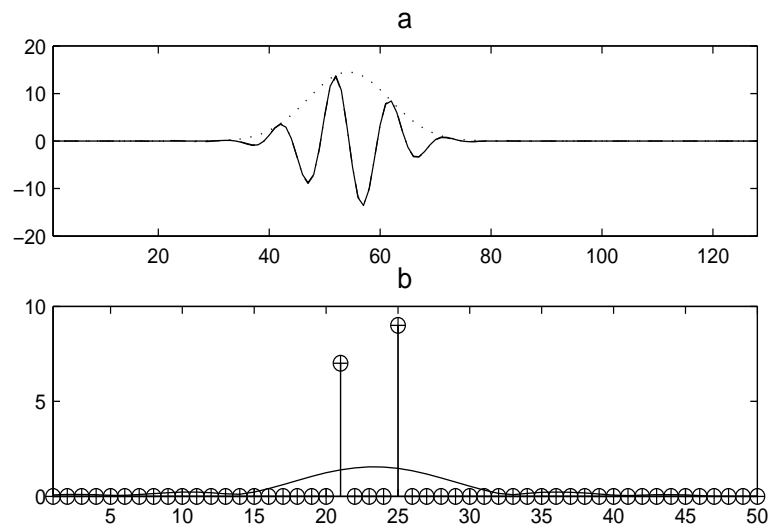


Fig. 2. Results of LSPC and LSTik methods. (a) RF signals and envelope. (b) Magnitude of medium responses. The true medium response is shown as circles. The LSPC and the LSTik results are shown with '+'s and solid line, respectively. Although only the magnitudes of the results are shown here, the LSPC method indeed accurately recovered both the real and imaginary parts of the solution.

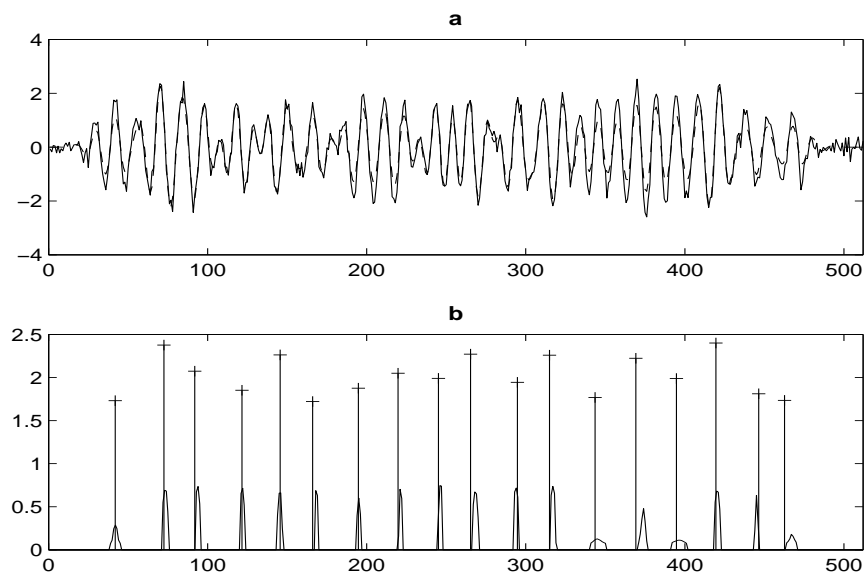


Fig. 3. Results of LSPC method with noisy data. (a) RF signals. The solid line is the observed signal and the dashed line is the recovered signal. (b) Magnitude of medium responses. The original medium response is shown as crosses and the solid line is the result of LSPC.

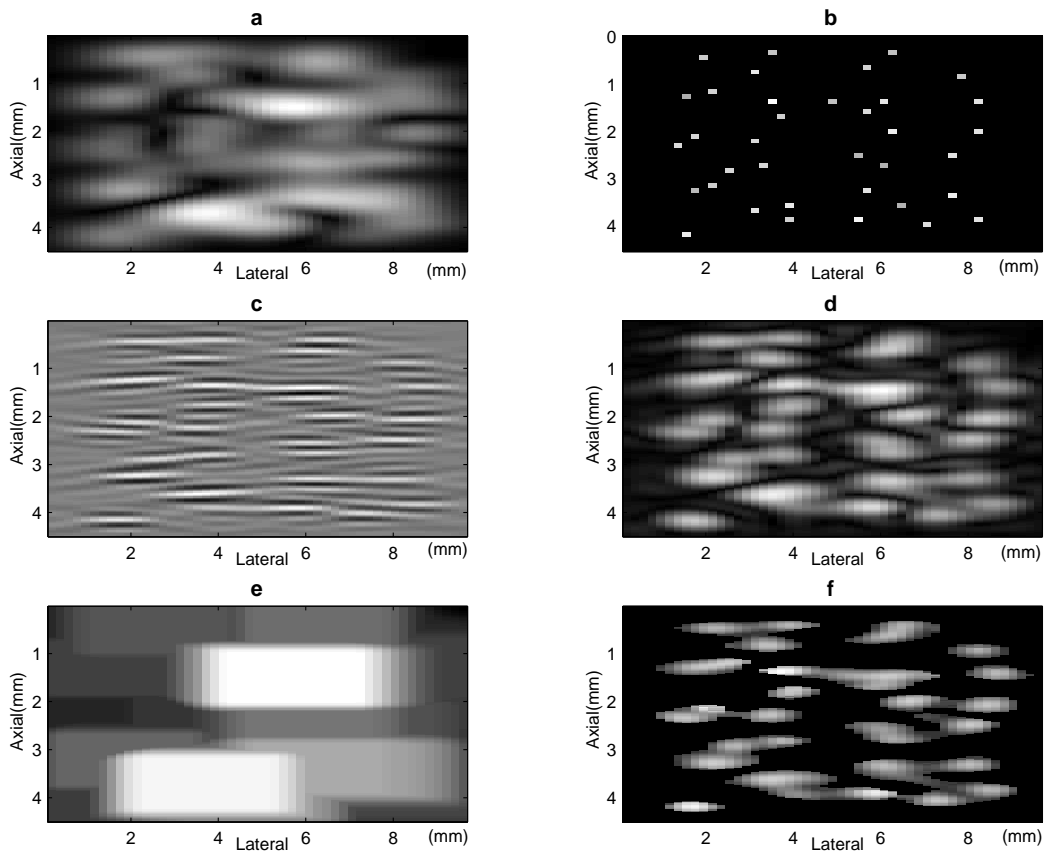


Fig. 4. The result of LSPC deconvolution of an image of randomly positioned scatterers. (a) Simulated B-mode image. (b) Original scatterer distribution. The intensity of the image represents the strength of scatterers. (c) Results of conventional Wiener filtering using only the real parts of the RF signal and pulse. (d) The magnitude of estimated medium response function using complex Wiener filtering given by equation (8). (e) The regularization parameter image, α , given by equation (20). (f) LSPC restored image after deconvolution with 40 iterations followed by median filtering. Finite support and soft thresholding are applied. The damping factor, K in equation (20), is 15, and the thresholding factor is chosen as 0.25.

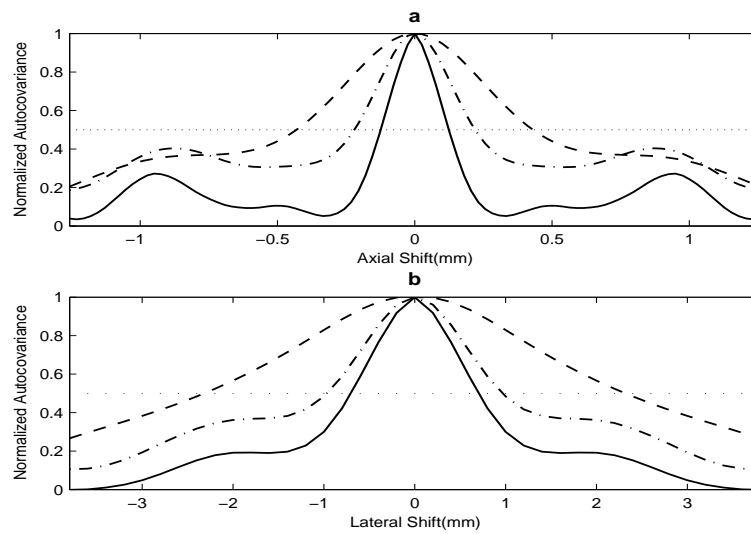


Fig. 5. Normalized image autocovariance functions before and after deconvolution. (a) Autocovariance functions with axial shift. (b) Autocovariance functions with lateral shift. The dashed line represents the function of the B-mode image (Fig. 4(a)), the dash-dot line is for the image after Wiener filtering (Fig. 4(d)), the solid line is for the image after LSPC deconvolution (Fig. 4(f)), and the dotted line marks the half maximum of the functions. The FWHM of the three autocovariance functions are $4.6mm$, $1.8mm$, and $1.4mm$ laterally, and $0.85mm$, $0.44mm$ and $0.23mm$ axially. These numbers show that the LSPC algorithm improves the image resolution over the observed B-mode image and the Wiener filtered image by factors of 3.3 and 1.3 laterally, and 3.7 and 1.9 axially.

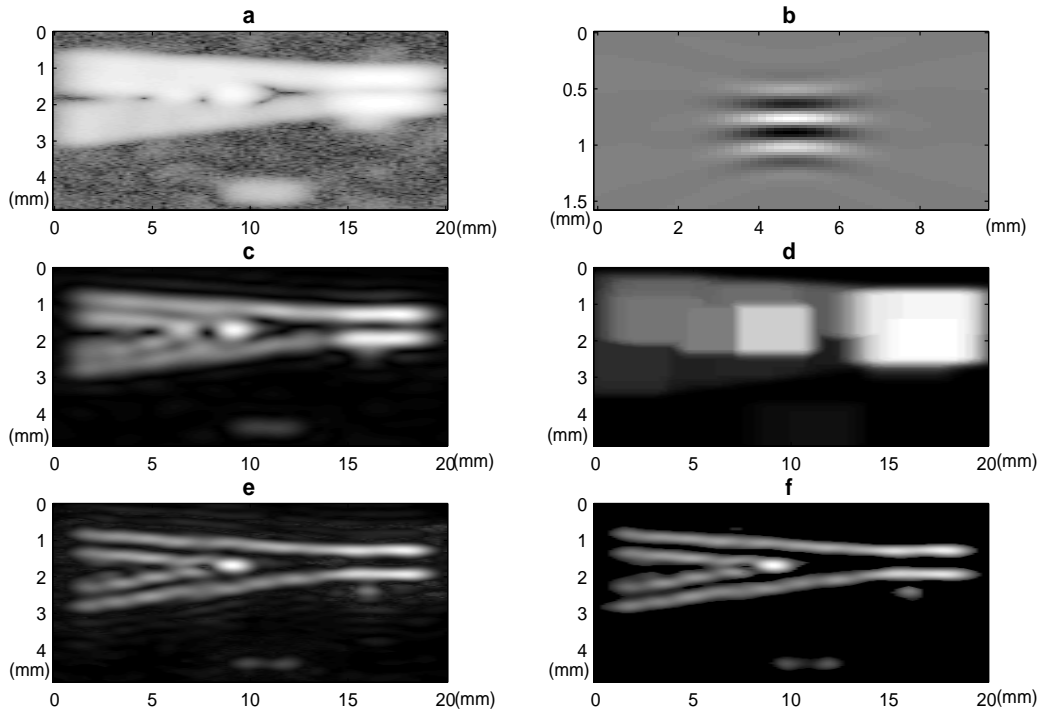


Fig. 6. The result of LSPC deconvolution of an noisy image of a blood vessel software phantom with speckle background. (a) Simulated B-mode image of a segment of blood vessel, a scatterer beneath the vessel on the right, and two scatterers near the bottom. The image is log-compressed to a 40dB dynamic range. The maximum intensity of the image is about 15, and the standard deviation of the additive Gaussian noise is 0.15. (b) The incident ultrasonic pulse. (c) The magnitude of estimated medium response function using complex Wiener filtering given by equation (8) that serves as the initial guess in the LSPC algorithm. (d) The regularization parameter image, α , given by equation (20). (e) and (f) are results of two implementations of the LSPC algorithm. Both use the Wiener filtered image as the initial guess and apply median filtering after iterations. (e) is obtained after 30 iterations without the use of finite support or soft thresholding. (f) is the result of 20 iterations with finite support and soft thresholding. The damping factor is 15, and the thresholding factor is chosen as 0.25.

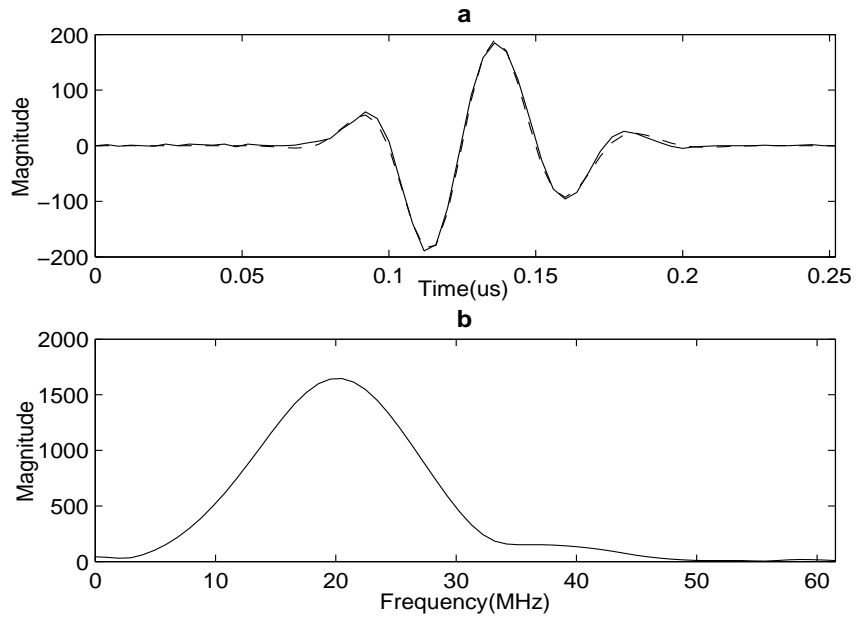


Fig. 7. The pulse of the V373 transducer and its spectrum. (a) The result of pulse fitting. The solid line is the measured echo signal and the dashed line is the curve-fitted pulse. (b) The magnitude of the FFT of the pulse.

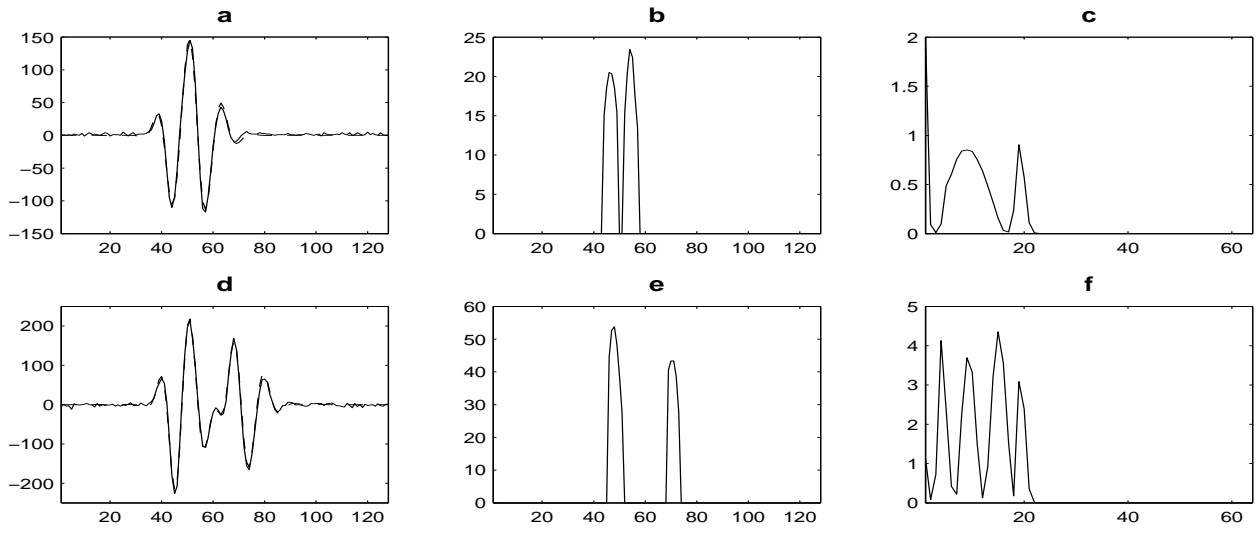


Fig. 8. Experimental results using plastic membranes with different thicknesses. Each row is a set of experimental data. The left column contains the RF echo signals. The results of deconvolution using LSPC method are shown in the middle column and the estimated power spectra (the low frequency half) of the medium responses in the right column.

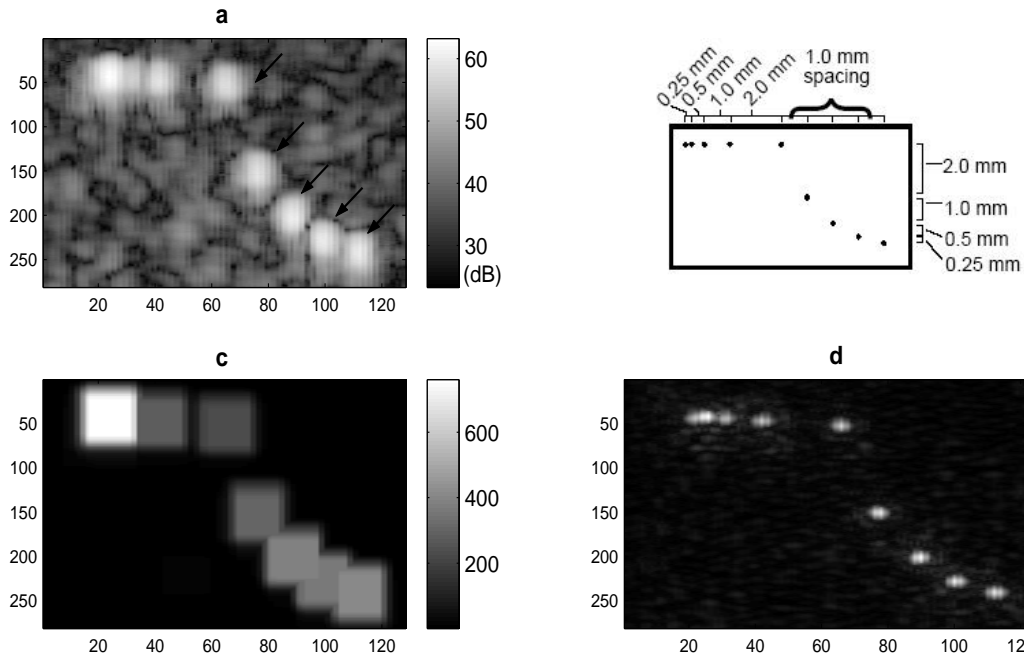


Fig. 9. Experimental result of LSPC algorithm. (a) Log-compressed B-mode phantom image acquired by a Siemens Antares medical ultrasound system. The phantom used is the RMI-404GS phantom. (b) The diagram of the targets in the imaged phantom. (c) The regularization parameter image, α , given by equation (20). (d) Deconvolved image after 40 LSPC iterations followed by median filtering. Neither finite support nor the soft thresholding technique was used in this experiment.

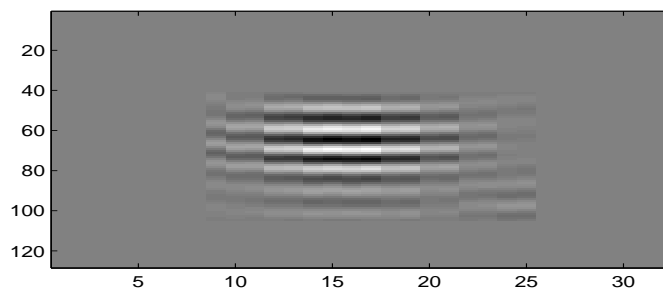


Fig. 10. Ultrasound pulse estimated from Fig. 9(a).